Title (100 characters)

Optoacoustics delineates murine breast cancer models displaying angiogenesis and vascular mimicry

Running title (50): Optoacoustic imaging in breast cancer models.

Authors:

Isabel Quiros-Gonzalez[1,2], Michal R Tomaszewski[1,2], Sarah J. Aitken[2,3], Laura Ansel-Bollepalli[1,2], Leigh-Ann McDuffus[2], Michael Gill[2], Lina Hacker[1,2], Joanna Brunker[1,2] and Sarah E. Bohndiek[1,2*].

Corresponding author:

* Sarah E. Bohndiek

seb53@cam.ac.uk

Affiliations:

[1] Department of Physics, University of Cambridge, JJ Thomson Avenue, Cambridge, CB3 0HE, U.K.

[2] Cancer Research UK Cambridge Institute, University of Cambridge, Robinson Way, Cambridge, CB2 0RE, U.K.

[3] Department of Histopathology, Addenbrooke's Hospital, Cambridge University Hospitals NHS Foundation Trust, Hills Road, Cambridge, CB2 0QQ, U.K.

Keywords: (Up to 12): Breast; Optoacoustic Imaging; Oestrogen; Oxygenation; Haemoglobin; Angiogenesis; Vascular Mimicry.

Abstract (200 words)

Background: Optoacoustic tomography (OT) of breast tumour oxygenation is a promising new technique, currently in clinical trials, which may help to determine disease stage and therapeutic response. However, the ability of OT to distinguish breast tumours displaying different vascular characteristics has yet to be established. The aim of the study is to prove OT as a sensitive technique for differentiating breast tumour models with manifestly different vasculatures.

Methods: Multispectral OT (MSOT) was performed in oestrogen-dependent (MCF-7) and oestrogen-independent (MDA-MB-231) orthotopic breast cancer xenografts. Total haemoglobin (THb) and oxygen saturation (SO_2^{MSOT}) were calculated. Pathological and biochemical evaluation of the tumour vascular phenotype was performed for validation.

Results: MCF-7 tumours show SO_2^{MSOT} similar to healthy tissue in both rim and core, despite significantly lower THb in the core. MDA-MB-231 tumours show markedly lower SO_2^{MSOT} with a significant rim-core disparity. Ex-vivo analysis revealed that MCF-7 tumours contain fewer blood vessels (CD31+) that are more mature (CD31+/aSMA+) than MDA-MB-231. MCF-7 presented higher levels of stromal VEGF and iNOS, with increased NO serum levels. The vasculogenic process observed in MCF-7 was consistent with angiogenesis, while MDA-MB-231 appeared to rely more on vascular mimicry.

Conclusion: OT is sensitive to differences in the vascular phenotypes of our breast cancer models.

Introduction

Management of breast cancer has improved significantly in the last two decades (Chen et al. 2014). Nonetheless, the high heterogeneity of the disease means some subtypes have good prognosis while others lack a successful treatment. As a result, breast cancer is still the third most common cause of cancer-related death in the EU (European Commission 2013). The different subtypes of breast cancer (Curtis et al. 2012) reflect different aspects of tumour biology, such as: cell of origin; hormone susceptibility; and receptor status. Factors such as angiogenesis, inflammatory and immune responses, and oxidative stress show significant cross-talk (Kundu & Surh 2012; Dewhirst et al. 2008) and play an important role in breast cancer progression and response to therapy (Bloom, H.J., Richardson 1957; Zardavas et al. 2015; Carmeliet & Jain 2000; Curtis et al. 2012). In particular, angiogenesis is considered a rate-limiting step in breast cancer progression and holds prognostic significance (Lam et al. 2016).

Imaging represents the standard-of-care for breast cancer detection and monitoring. X-ray and ultrasound are normally used together to improve the detection of the lesions, with magnetic resonance imaging (MRI) assisting with delineation of benign and malignant masses (Royal College of Radiologists 2010). However, there is presently no validated imaging technique to measure the functional effects of angiogenesis incorporated in the routine medical diagnosis of breast cancer.

In identifying a candidate imaging technique to overcome this limitation, intrinsic sensitivity to the functional effects of angiogenesis, including changes in oxygen supply and demand, hypoxia and perfusion, is preferable. The majority of existing clinical techniques need exogenous contrast agents: contrast enhanced ultrasound with microbubbles for perfusion and angiogenesis; dynamic contrast enhanced MRI with gadolinium for perfusion; and $H_2{}^{15}O$ or FMISO positron emission tomography for perfusion and hypoxia respectively (Mandic et al. 2016; Kenny 2016).

Potential for associated toxicity and side effects of contrast agents limits the recurrent use of these in the same patient (Rogosnitzky & Branch 2016). Some imaging techniques are not dependent on contrast agents, including Doppler ultrasound, Blood Oxygen Level Dependent (BOLD) and Oxygen-Enhanced (OE) MRI, but they lack sensitivity (Howe *et al*, 2001; Hallac *et al*, 2014). Imaging biomarkers of tumour oxygenation (O'Connor et al. 2016) could assist with: selection of appropriate therapies; definition of 'windows' for combination therapy; monitoring therapeutic response and reducing healthcare costs of targeted therapy (Kambadakone et al. 2015; Bohndiek et al. 2012).

Optoacoustic Tomography (OT) is an emerging imaging modality poised for clinical translation that combines the high contrast of optical imaging with the spatial resolution of ultrasound (Wang 2009). The absorption of pulsed laser energy in tissues generates pressure waves that can be detected by ultrasound transducers. OT is intrinsically sensitive to oxy- and deoxy-haemoglobin, adipose tissue and water content (Beard 2011), enabling detailed characterisation of tumour angiogenesis. Clinical OT operates at up to 5 cm depth in tissue (Menke 2015). Early results characterising breast lesions in clinical trials have shown increased haemoglobin content of lesions compared to normal breast parenchyma (Heijblom *et al*, 2015; Heijblom *et al*, 2016). The application OT using haemoglobin and other endogenous chromophores such as melanin or fat suggests that this technique this broad potential not only in the breast, but also for studying other superficial tumour types and beyond cancer, for example in inflammatory diseases (Zackrisson et al. 2014; McNally et al. 2016; Knieling et al. 2017). However, despite initial promise, there remain some limitations, one of them importantly being validation of the relationship between OT image features and underlying tumour biology.

To accelerate clinical translation of optoacoustic imaging as a routine diagnostic and monitoring tool, it is imperative to overcome this limitation and better establish the potential of OT, in our case, in clinical breast applications. We have

studied the angiogenic microenvironments generated in two breast cancer xenograft models: MCF-7 is an oestrogen-dependent tumour and MDA-MB-231 is an aggressive, oestrogen-independent tumour (Iorns et al. 2012). Here, we confirm that
60 the distinct angiogenic properties of these tumours can be sensitively detected through OT features and explain our findings through detailed characterisation of the tumour vascular phenotype.

Material and Methods

Cell lines

The human adenocarcinoma cell lines MCF-7 (Oestrogen Receptor +, OR+) and MDA-MB-231 (Oestrogen Receptor-, OR-) were obtained from the Cancer Research UK (CRUK) Cambridge Institute Biorepository from the University of Cambridge. Experiments were performed when cells were between passage 20-25 for both MCF-7 and MDA-MB-231. Authentication using Genemapper ID v3.2.1 (Genetica) by STR Genotyping (1/2015) showed 100% match with the reference sequence in both cases. Cells were maintained in DMEM supplemented by 10% of FBS at 37ºC in 5% CO_2. Oxygen consumption was measured using the MitoXpress Xtra Oxygen Consumption assay (see Supplementary Information).

Matrigel culture assay

A 24 well plate was pre-coated with Matrigel (growth factor reduced, SLS) and incubated for 30 min at 37ºC. The MCF-7 or MDA-MB231 cells were added to the pre-coated plate at 10^5 cells per well in DMEM-F12 medium supplemented with 2% FBS. Images were captured after 24 h using an inverted microscope (Nikon Eclipse TS100).

In vivo models

All animal procedures were conducted in accordance with project and personal licenses, reviewed by the Animal Welfare and Ethical Review Board at the CRUK Cambridge Institute, and issued under the United Kingdom Animals (Scientific Procedures) Act, 1986. All the procedures meet the standards required by the UKCCCR guidelines (Workman et al. 2010). Seven week-old immunodeficient female nude (BALB/c nu/nu) mice (n=20; Charles River) were inoculated orthotopically in the mammary fat pad of both flanks with 10^5 cells (either MCF-7, n=10 or MDA-MB-231,

n=10, random group assignment) in a final volume of 100 µL of 1:1 DMEM (GIBCO) and matrigel (BD). Power calculations to determine group size could not be performed in the first instance due to absence of previous data with this particular model and imaging modality, therefore the group size was based on our previous experience conducting in vivo optoacoustic tomography studies in other cell-line derived mouse tumour models (S. E. Bohndiek et al. 2015). For MCF-7, endogenous oestrogen levels were supplemented by surgical implantation of oestrogen pellet (0.72 mg/pellet, 90 days release; Innovative Research of America) in the scruff of the neck. In the MDA-MB-231 group, 1 mouse did not develop any tumours and 3 mice developed only 1 tumour; in the MCF-7 group, 1 mouse developed 1 tumour only. All tumour-bearing animals were entered into the study. For the tissue analysis, 4 animals were excluded from the MCF-7 cohort due to side effects caused by the oestrogen pellet (bladder obstruction and skin rash with scabs). Otherwise, all tumours were included in all analyses. Animals were kept in hermetic cages with individual air supply through an EPA filter to guarantee sterile conditions, in 12/12 hours ON/OFF light cycles, with enriched environment and food and water *ad libitum*.

All data acquisition was performed unblinded. Mice were imaged weekly after inoculation. Serum samples were taken at 3 and 6 weeks after tumours were detectable. Tumours were measured externally using vernier callipers (Figure S1A-D); according with local procedures, tumour volumes were calculated using the formula (A*b*b) being “A” the longest axis of the tumour and “b” the shortest. When the individual tumour sizes were over 1.5 cm diameter or overall tumour volume per mouse was over 10% of body weight, animals were euthanized by exsanguination and cervical dislocation as confirmation of death. Tumours were collected for histopathology and molecular biology assays. Immunohistochemistry stains included: CD31, alpha Smooth Muscle Actin (aSMA), oestrogen receptor (OR), Vascular Endothelial Growth Factor (VEGF), Carbonic Anhydrase IX (CA-IX), Periodic Acid-Schiff (PAS), Arginase and inducible Nitric Oxide Synthase (iNOS) as detailed in the

Supplementary Information. Western-blot for nitrotyrosine and VE-cadherin was performed according to standard methods, as was measurement of oxidative modification (see Supplementary Information).

Optoacoustic tomography

A commercial small animal MultiSpectral Optoacoustic Tomography (MSOT) system (inVision 256-TF; iThera Medical GmbH) was used in this study. The system has been described in detail elsewhere (Dima et al. 2014; Morscher et al. 2014). Briefly, a tunable (660–1300 nm) optical parametric oscillator (OPO), pumped by a nanosecond (ns) pulsed Nd:YAG laser, with 10Hz repetition rate and up to 7ns pulse duration is used for signal excitation. Light is delivered to the sample through a custom optical fibre assembly to obtain a uniform diffuse ring of illumination over the imaging plane. Coupling of the sample to the transducers is achieved using a water bath, filled with degassed and deionized water. An array of transducers covering an angle of 270° is used as the detector allowing tomographic reconstruction.

Mice were prepared according to our standard operating procedure (Joseph et al. 2017) and following UKCCCR guidelines (Workman et al. 2010). Briefly, mice were anaesthetized using <3% isoflurane in 100% oxygen and placed in a custom animal holder (iThera Medical), wrapped in a thin polyethylene membrane, with ultrasound gel (Aquasonic Clear, Parker Labs) used to couple the skin to the membrane. The holder was then placed within the MSOT system and immersed in degassed water maintained at 36°C for Hb and HbO_2 imaging acquisition. The animal respiratory rate was maintained in the range 70-80 bpm with ~1.5% isoflurane concentration for the entire scan. The animal holder was translated along the oral-caudal axis of the tumour and serial images every 0.5 mm were taken for all the animals. Images were acquired using 6 wavelengths between 700 nm and 950 nm, with an average of 10 pulses per wavelength. Each slice took 7 s to acquire, with overall imaging sessions lasting for a time ranging between 3-8 minutes.

Image and statistical analysis

All analysis was performed unblinded. Histopathological analysis of paraffin embedded tissue sections was performed on images scanned at 20x magnification using an Aperio ScanScope (Leica Biosystem) scanner, a whole tumour section of the wider tumour area was analysed. ROIs were drawn over the whole viable tumour area. The percentage of viable area was estimated in H&E sections (Figure S1E). The parameters measured were the following: CD31 staining= positive pixel count/ROI area; CD31 microvessel density= vessels marked by CD31/ROI area; ASMA positivity=positive pixel count /ROI area; Mast cell density= cells marked by toluidine blue/ROI area, CA-IX staining= positive pixel count/ROI area. Oesotrogen receptor status was confirmed in MCF-7 tumours using the percentage of positive nuclei (Figure S1F). CD31/PAS analyses were performed as follows, for same slide analysis 3 random fields per slide were studied, blood vessels were identified and percentage of CD31 positive blood vessels were identified by an expert. The quantification was performed blindly. In sequential adjacent tissue sections. Slides were scanned in an Axio Scan Z1 (ZEISS) and Halo Software (v2.1.1602) was used to synchronise the images. PAS positive blood vessels were identified by a histopathologist (S.J.A.) by drawing ROIs in 5 random fields per tumour sample (magnification 20x). An algorithm to quantify corresponding CD31 intensity analysed the presence of the protein in the blood vessel area.

For arginase and iNOS IHC quantification was performed using Image J software. Colour deconvolution for Haematoxylin counterstain of DAB (H-DAB) coordinates was applied; after 8-bit conversion the same threshold (122 and 107 for iNOS and arginase respectively) was applied to all the images. The positive pixels were counted using particle analysis. The average of the sum of the positive particles per field was the metric used for each sample and at least 3 fields (20x) were analysed per sample.

Optoacoustic tomography analysis was performed using ViewMSOT software (v3.6.0.119; iThera Medical GmbH). Model–based image reconstruction and multispectral processing were applied to retrieve the relative signal contributions of oxy- (HbO_2) and deoxy- (Hb) haemoglobin. Regions of Interest (ROIs) were drawn for the tomographic section in which the tumour presented the largest area (Figure 1A). Reference values from an ROI drawn around the abdominal aorta and vena cava were taken in the same anatomical plane, before they branch for the junction with the iliac bone (Figure 1A). ROIs were drawn over: the whole tumour; tumour rim (taken as 1 mm outer circumference of the tumour) and tumour core (the tumour area inside the 1 mm rim). OT measured ROI tumour areas correlated with tumour volume in both models (Figure S1G,H). Average and maximum intensities for HbO_2 and Hb were measured. Optoacoustic tomography is only able to accurately resolve absolute SO_2 if the recorded signal is directly related to the absorbed optical energy distribution, which requires knowledge of the light fluence distribution, system response and Grueneisen parameter (Cox et al. 2012). We therefore denote the oxygenation metric derived in this study as an apparent metric, SO_2^{MSOT} rather than absolute SO_2. SO_2^{MSOT} was computed as the ratio of HbO_2 to total haemoglobin signal in the ROI (THb = HbO_2+Hb).

Statistical analysis was performed using Prism (GraphPad). Each tumour was considered as an independent biological replicate. All data are shown as mean ± SEM unless otherwise stated. For end time point comparisons between the two cohorts for optoacoustic signals, histopathology results, plasma quantification, ELISA and western-blot, unpaired 2 tailed t-test was performed. For end time point comparisons between tumour rim and core within the same cohort, paired 2 tailed t-test was performed. For time course comparison within the same cohort, one-way ANOVA followed by Tukey's test for multiple comparisons when applicable and Pearson correlation was tested. Significance is assigned for p-values <0.05.

Results

Non-invasive assessment of tumour vasculature using optoacoustic tomography reveals different phenotypes between MCF-7 and MDA-MB-231 models.

The two breast cancer cell lines were chosen due to their biological differences: less aggressive, better differentiated phenotypes usually present a pronounced paracrine activity and recruit a more complex microenvironment, while the more aggressive, less differentiated types tend to acquire mesenchymal characteristics (D'Anselmi et al. 2013). Therefore, we expected these two cell lines present differences in vasculature when orthotopically implanted in mice.

Exemplar optoacoustic tomography (OT) image slices are shown in Figure 1A. Reproducibility based on the coefficient of variation for all OT metrics was tested over 3 repeated measurements made over 48 hours (Figure S2A). As we assessed previously in healthy organs, oxygen saturation (SO_2^{MSOT}) and total haemoglobin (THb) exhibit a lower coefficient of variation compared to the direct measurements of oxy- and deoxy-haemoglobin (Hb and HbO_2) (Joseph et al. 2017) hence we focused on the measurement of SO_2^{MSOT} and THb for the remainder of the analysis. The SO_2^{MSOT} in established MDA-MB-231 tumours was significantly lower than both MCF-7 tumours and the reference region (Figure 1B; SO_2^{MSOT} = 46±1% vs. 55±2 and 55±3% for the reference region in the same mice respectively). The SO_2^{MSOT} in MCF-7 tumours was equivalent to the reference region in the same mice. The THb in the tumour is significantly lower than in the reference and no difference was observed between the tumours generated by both models (Figure 1C).

Since OT is fast, non-invasive and label free, longitudinal monitoring of tumour development is possible. We performed weekly imaging sessions in all mice following tumour inoculation. The different oxygenation levels observed in the established tumours is also discernible early in the time course analysis and

maintains throughout tumour growth. A trend towards decreasing SO_2^{MSOT} (Figure S2B) is confirmed when the SO_2^{MSOT} of the MCF-7 tumour is corrected by the SO_2^{MSOT} of the reference (Figure S2C, Pearson p=0.001), accounting for any drifts in OT performance over longer term studies. THb is not affected during tumour growth (Figure S2E). No change in SO_2^{MSOT} or THb is observed in the MDA-MB-231 tumours throughout the time course.

Optoacoustic tomography detects spatial variation in vascular maturity.

Tumour oxygenation generally decreases with depth, as the outer rim of the tumour can be well oxygenated by diffusion but the core of the tumour experiences perfusion- and diffusion-limited access to oxygen (Hendriksen et al. 2009). We thus hypothesised that OT would detect a lower total haemoglobin and oxygen saturation in the core of our tumour models. To test this hypothesis, we drew additional regions of interest to delineate two areas of the tumour (Figure 2A): the rim, defined as the perimeter area of 1 mm depth into the tumour; and the core, the rest of the tumour area after the rim has been excluded. Both tumour models present a significant reduction in THb between the rim and the core (Figure 2B; MCF-7 THb = 14.4±1.4 rim vs 7.8±0.6 core; MDA-MB-231 THb = 15.0±1.1 rim vs 8.7±0.9 core). However, only MDA-MB-231 tumours show a significant reduction in SO_2^{MSOT} between the rim and the core (Figure 2C; MDA-MB-231 SO_2^{MSOT} = 47.7±2.1 rim vs 38.0±2.3 core). The underlying Hb and HbO_2 values (Figure S3A,B) show comparable trends.

Given the different growth rates observed for the two breast tumour models (Figure S1A-D), we also performed a size-matched analysis of this spatial heterogeneity. We divided the tumours into small (<10 mm^2), medium (10-20 mm^2), large (20-30 mm^2) and very large (>30 mm^2) size classes according to ROI area measured by OT (Figure 2D), which correlates with tumour volume (Figure S1G,H). Equal numbers of “large” MCF-7 and MDA-MB-231 tumours were available, so we chose this group for our size-matched analysis. The rim-core behaviour found within

each model in the whole cohort analysis persisted in the size-matched analysis (Figure 2E,F). When comparing the THb between models (i.e. MCF-7 rim compared to MDA-MB-231 rim; MCF-7 core compared to MDA-MB-231 core) we observed no significant differences (Figure 2E). The SO_2^{MSOT} was similar for the rims of both groups while the core of MCF-7 had significantly higher SO_2^{MSOT} than the core of MDA-MB-231 tumours of similar size (Figure 2F). Again, the underlying Hb and HbO_2 values (Figure S3C,D) confirm these findings. The dynamic of the oxygenation in rim and core was also analysed over time (Figure S3E). The behaviour was similar to previous result, with the average oxygenation being higher in MCF-7 than in MDA-MB-231. The levels of oxygenation in MCF-7 are higher in the core at the earlier time points but the rim and core become comparable at later time points. MDA-MB-231 tumours showed similar oxygenation in the rim compared to the core in the first stages of tumour development, with disparity arising later. Taken together, these findings show MCF-7 tumours exhibit high oxygenation, similar to healthy tissue, indicating a functional vasculature in both their rim and core; conversely, MDA-MB-231 tumours show a poorer oxygenation overall, likely driven by their poorly oxygenated core.

Histological assessment proves the higher maturity of the vessels in MCF-7 tumours.

OT assessment of THb and SO_2^{MSOT} relies on the presence of blood within the tumour mass; consequently, differences in vascular density and function would be expected to modify these imaging biomarkers. Mature, functional blood vessels are supported by an effective vascular network that includes at least two cell types: endothelial cells, forming the blood vessel wall; and pericytes, providing structural coverage to resist the blood flow. In order to establish the underlying vascular density and function in the two breast tumour models, we examined the endothelial and pericyte layers using IHC for CD31 and α-Smooth Muscle Actin (ASMA) respectively

(Figure 3A). Both overall CD31 staining and microvessel density (MVD) were significantly higher in MDA-MB-231 tumours (Figure 3B,C; CD31: 0.04±0.006 MCF-7 vs 0.21±0.03 MDA-MB-231; MVD: $5.3x10^{-5}$±$0.4x10^{-5}$ MCF-7 vs $1.1x10^{-4}$±$0.7x10^{-5}$ MDA-MB-231). The vessel wall thickness was significantly higher in MCF-7 tumours (Figure 3D; 2.38±0.05 MCF-7 vs 2.14±0.03 MDA-MB-231), which also showed a much higher staining of ASMA co-localised with CD31 (Figure 3E; $3.4x10^{-7}$±$1.1x10^{-7}$ MCF-7 vs $0.6x10^{-7}$±$0.2x10^{-7}$ MDA-MB-231). While MCF-7 tumours exhibit mostly strong areas stained by CD31 and always surrounded by strong ASMA staining, MDA-MD-231 tumours showed positive low staining of CD31 in areas where no ASMA staining was detected, probably representing the immature vasculature generated in this tumour model (Figure 3A, arrowheads), These results indicate that the blood vessels in MCF-7 tumours present pericyte or media layer, being more mature compared to MDA-MB-231 tumours, which contain poorly developed blood vessels.

The angiogenic-related microenvironment is different between both models.

In order to characterise the origin of the different vasculature we studied different aspects that are able to influence the angiogenesis process. We sought to better understand the connection between the non-invasive OT imaging data and the underlying tumour biology relating to vessel formation, including hypoxia and inflammation. The relationship between blood oxygenation as measured by OT, and tissue oxygenation is affected by the vascular structure and metabolism of the tumour. Therefore, we first assessed the basal oxygen consumption of both cell lines, finding that the oxygen consumption in MCF-7 cells is significantly higher than in MDA-MB-231 cells (Figure 4A; 8.07±1.33 MCF-7 vs 4.03±0.58 MDA-MB-231). We then confirmed that MDA-MB-231 tumours also exhibit higher levels of hypoxia, by assessing tumour expression of Carbon Anhydrase IX (CA-IX), a protein up-regulated in hypoxic conditions (Figure 4B; 0.53±0.04 MCF-7 vs 0.73±0.02 MDA-MB-

231). This reinforces our vascular IHC analysis, indicating that the lower levels of blood oxygenation in the MDA-MB-231 tumours is likely due to the lower vascular maturity, which limits oxygen delivery to the tumour tissue.

Next, we determined the tumour and serum levels of vascular endothelial growth factor (VEGF), one of the most important pro-angiogenic factors (Hoeben et al. 2004). VEGF can be secreted by stromal cells, due to inflammation, and directly by tumour cells under hypoxia. The local levels of VEGF in the tumour assessed by IHC were significantly higher in MCF-7 than in MDA-MB-231 tumours (Figure 4C; 0.63±0.06 MCF-7 vs 0.55±0.03 MDA-MB-231). To elucidate the source of VEGF, we measured the serum levels of human VEGF (hVEGF), coming from the tumour cells, and mouse VEGF (mVEGF), coming from host tissue. Although the levels of hVEGF are similar in both tumour models, mVEGF is significantly increased in the serum of mice bearing MCF-7 (Figure 4D; 86.2±10.6 MCF-7 vs 15.7±6.2 MDA-MB-231), pointing to the stromal compartment as the main source of VEGF in MCF-7 model. Interestingly, another important mediator of inflammation and endothelial homeostasis, nitric oxide (NO), was also significantly increased in serum of mice bearing MCF-7 tumours (Figure 4E; 210.6±45.9 MCF-7 vs 40.8±4.8 MDA-MB-231). Since NO can be produced by macrophages, we assessed by IHC iNOS expression, to denote type 1 macrophages and arginase expression, to denote type 2 macrophages (He & Carter 2015). The levels of these proteins (both of mouse origin) were significantly higher in MCF-7 tumours (Figure 4F; iNOS: 3284±888 MCF-7 vs 850±182 MDA-MB-231; Arginase: 10111±2542 MCF-7 vs 1002±298 MDA-MB-231). This increase occurs without any coincident increase in oxidative stress (Figure S4). Taken together these results suggest that the main driving force for angiogenesis in MCF-7 tumours is inflammation rather than local hypoxic stimuli.

Given the lack of macrophage infiltration and low levels of mVEGF, an inflammatory stimulus could not explain the vascular features of the MDA-MB-231 tumours. Furthermore, despite a high density of tumour blood vessels, MDA-MB-231

tumours show significantly lower VEGF staining. To clarify which vascular pathway was activated in these cells, we checked the ability of these cells to trans-differentiate into endothelial-like tubular structures in matrigel, a process referred to as 'vascular mimicry' (VM), which has been previously reported. In line with previous results, our MDA-MB-231 cells form such structures after 24h of 3D matrigel culture (Figure 5A). We analysed the *in vivo* capacity of VM in both cell lines by studying the expression of CD31 and PAS in blood vessels. Vessels derived by VM are PAS positive but do not express CD31 (Maniotis et al. 1999). We identified PAS-positive blood vessels and then quantified their positivity for CD31 staining (Figure 5B; see also Figure S5). We observed significantly fewer CD31+/PAS+ vessels in MDA-MB-231 tumours compared with MCF-7 derived tumours (Figure 5C). The MDA-MB-231 tumours also showed detectable expression of VM marker VE-Cadherin (Williamson et al. 2016) (Figure 5D; positive in 8 of 15 tumours compared to 0 of 8 tumours in MCF-7). The presence of vascular mimicry that we have identified in MDA-MB-231 tumours may explain in part their poorer overall oxygenation.

Discussion

The aim of this study was to define whether OT can detect differences in the vasculature and oxygenation of two biologically different breast cancer xenografts. We sought to determine whether the features defined by OT were connected with the underlying vascular phenotype. To achieve these aims, we used two different breast cancer cell lines exemplifying different stages of the breast cancer evolution. We studied the functional OT image information relating to the vasculature, including changes in haemoglobin concentration (THb) and oxygenation (SO_2^{MSOT}) and evaluated the biological features that underlie these features.

Globally, our results confirm OT is sufficiently sensitive to differentiate *in vivo* and in real-time the vasculature features of the tumours generated by two breast cancer cell lines as representing different stages of the disease. Our oestrogen dependent MCF-7 tumours showed an average oxygenation similar to normal blood vasculature, which was also much higher than MDA-MB-231 tumours. The average oxygenation of MCF-7 tumour tissue decreased over time as the tumour developed, whereas in MDA-MB-231 tumours, oxygenation remained low across the time course. The work from Wilson et al described alterations in THb and increased SO_2 during initiation, promotion and progression in a transgenic breast cancer model (Wilson et al. 2014). They also described a reduction in basal systemic haemoglobin levels in the mice bearing invasive tumours compared to the normal and hyperplasia bearing mice. Increases in SO_2 and THb that were observed during hyperplasia and the malignant transformation are not recapitulated in our model, but consistent with our results they describe a decrease SO_2 and THb during the in situ carcinoma and invasive disease. In addition, their ex-vivo analysis actually indicated increased vessel density in the invasive tumours, as we show here for the more aggressive MDA-MB-231 tumours compared to MCF-7.

Both tumour types showed a pronounced rim-core effect, with more haemoglobin present in the rim of the tumours. MCF-7 tumours were similarly

oxygenated in both the rim and core, whereas MDA-MB-231 tumours had a poorly oxygenated tumour core. The rim-core effect in OT and histopathology data for MDA-MB-231 observed here was consistent with previous work by Bar-Zion *et al*, where higher THb and SO_2 values were shown in tumour rims (Bar-Zion *et al*, 2016).

Comparing the vascular phenotype of these tumour models using immunohistochemistry, we found that while MDA-MB-231 tumours had a far higher microvessel density, but their vessels were poorly developed, with little pericyte coverage. These findings explain our OT image features, particularly the low oxygenation measured in MDA-MB-231 tumours, as vessels with low pericyte coverage lack vasoactivity and increased pericyte coverage has previously been linked to tumour oxygenation (S. Bohndiek et al. 2015). Furthermore, the similar OT haemoglobin signal between the tumour types indicates many of the vessels present in MDA-MB-231 tumours are likely to be non-functional.

To understand the origins of the differing vascular phenotypes of these tumours, we examined their hypoxic and inflammatory phenotypes. The biochemical pattern shown by MCF-7 tumours, with high levels of VEGF and NO and positive expression of proteins involved in macrophage function, indicates activation of the angiogenic pathway and also the involvement of inflammation and/or endothelial cells. Conversely, MDA-MB-231 tumours appear less dependent on angiogenesis, with expression of human VE-cadherin measured in tumour extracts. They are also characterised by PAS+ blood vessels negative for CD31 expression, indicating vascular mimicry. Such features of vasculogenesis in these cell lines have previously been described *in vitro* (Cui et al. 2015) and our *in vivo* results in tumour tissue support their findings. However, the presence of a large number of CD31+ vessels in our MDA-MB-231 tumours may be considered unusual, as previous work suggests that vessels formed by vascular mimicry do not express this endothelial marker (Wagenblast et al. 2015). The presence of CD31+ vessels could be due to the co-

existence of both vascular mimicry and angiogenesis, or due to vascular mimicry induced by macrophages, in which the presence of CD31+ cells has been recently described (Barnett et al. 2016). Nonetheless, the deficient structure of vessels arising from vascular mimicry would impair exchange of oxygen from haemoglobin, which may provide part of the explanation for differences in oxygenation measured with OT. To our knowledge, this is the first time that OT has been used in tumours presenting features of vascular mimicry and reinforces the potential application of OT to monitor vasculogenic processes in tumours (Soda et al. 2013; Weathers & De Groot 2014). Nonetheless, further experiments have to be performed to confirm whether OT can be more broadly applied to discriminate vascular mimicry and angiogenesis.

There remain some key limitations to our study. Firstly, we examine an orthotopic xenograft model system using only two cell lines, representing oestrogen-dependent and independent disease but there are other subtypes that are relevant for the disease. The absence of an adaptive immune system in the nude mice used for the study may also impact tumour development and the resulting vascular phenotype. Our findings should therefore be further verified in additional models, including transgenic or patient-derived tumour models, prior to being evaluated in a clinical setting. Secondly, we analyse only relative values of haemoglobin concentration and oxygenation, rather than absolute values. To derive absolute values would require compensation for differential attenuation of the full range of wavelengths used via light fluence correction of the OT data; application of light fluence correlation *in vivo* is the subject of current research (Brochu et al. 2015) but is not yet validated for routine use. As a result, only relative values were presented here.

Clinical applications of OT in breast cancer appear promising compared to existing clinical imaging modalities, particularly when applied to dense breasts (Heijblom *et al*, 2015; Heijblom *et al*, 2016). Limitations with sensitivity and specificity remain, which may be influenced by the type of detector (hand held, frame with

compressing plates or cup shape) and the available wavelengths for imaging. Here, we confirmed that OT image data acquired in the wavelength range from 700 to 950 nm to determine blood concentration and oxygenation reflects the underlying vascular phenotype of two breast tumour models, moving OT one step closer to validation as an imaging modality in breast cancer. Future studies will be needed to elucidate whether OT meets the clinical need for an accurate, fast and affordable tool to provide validated imaging biomarkers of tumour angiogenesis.

Acknowledgements

IQG would like to thank John Stingl and Al Russell for their help to develop the animal models as well as Neal Burton from iThera Medical for his technical support and intellectual input. IQG and SEB thank CRUK Cambridge Institute Core Facilities for their support, including: the BRU; Light Microscopy; Biorepository; Preclinical Imaging and the Histopathology Core (Jo Arnold, Jodi Miller, Cara Walters and Bev Wilson). This work was supported by the EPSRC-CRUK Cancer Imaging Centre in Cambridge and Manchester (C197/A16465), Cancer Research UK (C14303/A17197, C47594/A16267) and the European Union's Seventh Framework Programme (FP7/2007-2013) under grant agreement n° FP7-PEOPLE-2013-CIG-630729.

Conflicts of interest:

IQG, MRT and SEB received conference travel funding from iThera Medical.

Key References:

Bar-Zion, A. et al., 2016. Functional flow patterns and static blood pooling in tumors revealed by combined contrast-enhanced ultrasound and photoacoustic imaging. *Cancer Research*, 76(15), pp.4320–4331.

Barnett, F. et al., 2016. Macrophages form functional vascular mimicry channels in vivo. *Scientific reports*, (6).

Beard, P., 2011. Biomedical photoacoustic imaging. *Interface focus*, 1(4), pp.602–31. Available at: http://www.pubmedcentral.nih.gov/articlerender.fcgi?artid=3262268&tool=pmcentrez&rendertype=abstract.

Bloom, H.J., Richardson, W.W., 1957. Histological grading and prognosis in breast cancer; a study of 1409 cases of which 359 have been followed for 15 years. *Br J Cancer*, 3(11), pp.359–77.

Bohndiek, S. et al., 2015. Photoacoustic tomography detects early vessel regression and normalization during ovarian tumor response to the anti-angiogenic therapy Trebananib. *Journal of Nuclear Medicine*, 215.

Bohndiek, S.E. et al., 2012. Hyperpolarized 13C spectroscopy detects early changes in tumor vasculature and metabolism after VEGF neutralization. *Cancer Research*, 72(2), pp.854–864.

Bohndiek, S.E. et al., 2015. Photoacoustic Tomography Detects Early Vessel Regression and Normalization During Ovarian Tumor Response to the Antiangiogenic Therapy Trebananib. *Journal of nuclear medicine : official publication, Society of Nuclear Medicine*, 56(12), pp.1942–7. Available at: http://www.ncbi.nlm.nih.gov/pubmed/26315834.

Brochu, F.M. et al., 2015. Light fluence correction for quantitative determination of

tissue absorption coefficient using multi-spectral optoacoustic tomography. In *Proc. of SPIE*. p. 95390Z–1–95390Z–8.

Carmeliet, P. & Jain, R.K., 2000. Angiogenesis in cancer and other diseases. *Nature*, 407(6801), pp.249–257.

Chen, L. et al., 2014. Trends in 5-year survival rates among breast cancer patients by hormone receptor status and stage. *Breast Cancer Research and Treatment*, 147(3), pp.609–616.

Cox, B. et al., 2012. Quantitative spectroscopic photoacoustic imaging: a review. *J. Biomed. Opt.*, 17(6), p.61202.

Cui, Y. et al., 2015. Claudin-4 is required for vasculogenic mimicry formation in human breast cancer cells. *Oncotarget*, 6(13), pp.11087–97.

Curtis, C. et al., 2012. The genomic and transcriptomic architecture of 2,000 breast tumours reveals novel subgroups. *Nature*, 486(7403), pp.346–52. Available at: http://www.pubmedcentral.nih.gov/articlerender.fcgi?artid=3440846&tool=pmcentrez&rendertype=abstract.

D'Anselmi, F. et al., 2013. Microenvironment promotes tumor cell reprogramming in human breast cancer cell lines. *PLoS ONE*, 8(12).

Dewhirst, M.W., Cao, Y.T. & Moeller, B., 2008. Cycling hypoxia and free radicals regulate angiogenesis and radiotherapy response. *Nature Reviews Cancer*, 8(8), pp.425–437.

Dima, A., Burton, N.C. & Ntziachristos, V., 2014. Multispectral optoacoustic tomography at 64, 128, and 256 channels. *Journal of biomedical optics*, 19(3), p.36021. Available at: http://www.ncbi.nlm.nih.gov/pubmed/24676383.

European Commission, 2013. Causes of death-standarished death rate 2013. Available at: http://ec.europa.eu/eurostat/statistics-

explained/index.php/File:Causes_of_death_—_standardised_death_rate,_2013.png.

Hallac, R.R. et al., 2014. Correlations of noninvasive BOLD and TOLD MRI with pO2 and relevance to tumor radiation response. *Magnetic Resonance in Medicine*, 71(5), pp.1863–1873.

Hatfield, S.M. et al., 2015. Immunological mechanisms of the antitumor effects of supplemental oxygenation. *Science translational medicine*, 7(277), p.277ra30. Available at: http://www.ncbi.nlm.nih.gov/pubmed/25739764%5Cnhttp://www.pubmedcentral.nih.gov/articlerender.fcgi?artid=PMC4641038.

He, C. & Carter, A.B., 2015. The Metabolic Prospective and Redox Regulation of Macrophage Polarization. *Journal of clinical & cellular immunology*, 6(6), pp.1–16. Available at: http://www.pubmedcentral.nih.gov/articlerender.fcgi?artid=4780841&tool=pmcentrez&rendertype=abstract.

Heijblom, M. et al., 2015. Photoacoustic image patterns of breast carcinoma and comparisons with Magnetic Resonance Imaging and vascular stained histopathology. *Scientific reports*, 5(February), p.11778. Available at: http://www.ncbi.nlm.nih.gov/pubmed/26159440.

Heijblom, M. et al., 2016. The state of the art in breast imaging using the Twente Photoacoustic Mammoscope: results from 31 measurements on malignancies. *European Radiology*, 26(11), pp.3874–3887.

Hendriksen, E.M. et al., 2009. Angiogenesis, hypoxia and VEGF expression during tumour growth in a human xenograft tumour model. *Microvascular Research*, 77(2), pp.96–103.

Hoeben, A. et al., 2004. Vascular endothelial growth factor and angiogenesis.

Pharmacological reviews, 56(4), pp.549–580.

Howe, F.A. et al., 2001. Issues in flow and oxygenation dependent contrast (FLOOD) imaging of tumours. *NMR in biomedicine*, 14(7–8), pp.497–506.

Iorns, E. et al., 2012. A new mouse model for the study of human breast cancer metastasis. *PLoS One*, 7, p.e47995. Available at: http://dx.doi.org/10.1371/journal.pone.0047995%5Cnhttp://www.ncbi.nlm.nih.gov/pmc/articles/PMC3485320/pdf/pone.0047995.pdf.

Joseph, J. et al., 2017. Evaluation of Precision in Optoacoustic Tomography for Preclinical Imaging in Living Subjects. *Journal of Nuclear Medicine*, 58(5), pp.807–814. Available at: http://jnm.snmjournals.org/lookup/doi/10.2967/jnumed.116.182311.

Kallinowski, F. et al., 1989. Blood flow, metabolism, cellular microenvironment, and growth rate of human tumor xenografts. *Cancer research*, 49(14), pp.3759–64. Available at: http://www.ncbi.nlm.nih.gov/pubmed/2736517.

Kambadakone, A. et al., 2015. CT perfusion as an imaging biomarker in monitoring response to neoadjuvant bevacizumab and radiation in soft-tissue sarcomas: comparison with tumor morphology, circulating and tumor biomarkers, and gene expression. *AJR. American journal of roentgenology*, 204(1), pp.W11–W8.

Kenny, L., 2016. The Use of Novel PET Tracers to Image Breast Cancer Biologic Processes Such as Proliferation, DNA Damage and Repair, and Angiogenesis. *Journal of nuclear medicine : official publication, Society of Nuclear Medicine*, 57 Suppl 1(Supplement 1), p.89S–95S. Available at: http://www.ncbi.nlm.nih.gov/pubmed/26834108.

Knieling, F. et al., 2017. Multispectral Optoacoustic Tomography for Assessment of Crohn's Disease Activity. *New England Journal of Medicine*, 376(13), pp.1292–1294. Available at: http://www.nejm.org/doi/10.1056/NEJMc1612455.

Kundu, J.K. & Surh, Y.J., 2012. Emerging avenues linking inflammation and cancer. *Free Radical Biology and Medicine*, 52(9), pp.2013–2037.

Lam, S.W. et al., 2016. Angiogenesis- and hypoxia-associated proteins as early indicators of the outcome in patients with metastatic breast cancer given first-line bevacizumab-based therapy. *Clinical Cancer Research*, 22(7), pp.1611–1620.

Mandic, L. et al., 2016. Molecular Imaging of Angiogenesis in Cardiac Regeneration. *Current Cardiovascular Imaging Reports*, 9(10).

Maniotis, a J. et al., 1999. Vascular channel formation by human melanoma cells in vivo and in vitro: vasculogenic mimicry. *The American journal of pathology*, 155(3), pp.739–52. Available at: http://www.pubmedcentral.nih.gov/articlerender.fcgi?artid=1866899&tool=pmcentrez&rendertype=abstract.

McNally, L.R. et al., 2016. Current and emerging clinical applications of multispectral optoacoustic tomography (MSOT) in oncology. *Clinical Cancer Research*, 22(14), pp.3432–3439.

Menke, J., 2015. Photoacoustic breast tomography prototypes with reported human applications. *European Radiology*, 25(8), pp.2205–2213.

Morscher, S. et al., 2014. Semi-quantitative multispectral optoacoustic tomography (MSOT) for volumetric PK imaging of gastric emptying. *Photoacoustics*, 2(3), pp.103–110.

O'Connor, J.P.B. et al., 2016. Imaging biomarker roadmap for cancer studies. *Nature Reviews Clinical Oncology*.

Palazon, A. et al., 2014. HIF Transcription Factors, Inflammation, and Immunity. *Immunity*, 41(4), pp.518–528.

Priya, M. et al., 2015. Monitoring breast tumor progression by photoacoustic measurements: a xenograft mice model study. *Journal of Biomedical Optics*, 20(10), p.105002. Available at: http://biomedicaloptics.spiedigitallibrary.org/article.aspx?doi=10.1117/1.JBO.20.10.105002.

Rogosnitzky, M. & Branch, S., 2016. Gadolinium-based contrast agent toxicity: a review of known and proposed machanisms. *Biometals*, 29, pp.365–376.

Royal College of Radiologists, 2010. *In breast cancer specifically both ultrasound and X-ray are used to improve detection.*,

Soda, Y. et al., 2013. Mechanisms of neovascularization and resistance to anti-angiogenic therapies in glioblastoma multiforme. *Journal of Molecular Medicine*, 91(4), pp.439–448.

Solaini, G. et al., 2010. Hypoxia and mitochondrial oxidative metabolism. *Biochimica et biophysica acta*, 1797(6–7), pp.1171–7. Available at: http://www.sciencedirect.com/science/article/pii/S0005272810000575.

Wagenblast, E. et al., 2015. A model of breast cancer heterogeneity reveals vascular mimicry as a driver of metastasis. *Nature*, 520(7547), pp.358–362. Available at: http://www.nature.com/doifinder/10.1038/nature14403.

Wang, L.V., 2009. Multiscale photoacoustic microscopy and computed tomography. *Nature Photonics*, 9(3), pp.503–509.

Weathers, S.P. & De Groot, J., 2014. Resistance to antiangiogenic therapy. *Current Neurology and Neuroscience Reports*, 14(5).

Williamson, S.C. et al., 2016. Vasculogenic mimicry in small cell lung cancer. *Nature Communications*, 7, p.13322. Available at: http://www.nature.com/doifinder/10.1038/ncomms13322.

Wilson, K.E. et al., 2014. Multiparametric spectroscopic photoacoustic imaging of breast cancer development in a transgenic mouse model. *Theranostics*, 4(11), pp.1062–1071.

Workman, P. et al., 2010. Guidelines for the welfare and use of animals in cancer research. *British Journal of Cancer*, 102(11), pp.1555–1577. Available at: http://www.nature.com/doifinder/10.1038/sj.bjc.6605642.

Zackrisson, S., Van De Ven, S.M.W.Y. & Gambhir, S.S., 2014. Light in and sound out: Emerging translational strategies for photoacoustic imaging. *Cancer Research*, 74(4), pp.979–1004.

Zardavas, D. et al., 2015. Clinical management of breast cancer heterogeneity. *Nature reviews. Clinical oncology*, pp.1–14. Available at: http://www.nature.com/doifinder/10.1038/nrclinonc.2015.73.

Main Text Figure Legends

Figure 1: Optoacoustic tomography reveals oestrogen-independent MDA-MB-231 tumours have poorer oxygenation than oestrogen-dependent MCF-7 tumours and healthy tissue. (A) Regions of interest (yellow outline) were drawn in the optoacoustic tomography slice at which the tumour area burden was highest. A region containing the aorta and inferior vena cava was used as a baseline reference in normal tissue. Representative images of tumors showing the spatial distribution of (B) tumour oxygenation (SO_2^{MSOT}) and (C) total hemoglobin (THb). Quantification graphs are shown on the right, data were extracted from all regions of interest, showing a significantly higher oxygenation in MCF-7 compared to MDA-MB-231 (B) tumours and a decrease in THb (C). n^{MCF-7} =11; n^{231} =16, data expressed as mean±SEM. * $p<0.05$, **** $p<0.0001$. Statistical significance was assessed by paired 2-tailed t-test within a single tumour type and by unpaired 2-tailed t-test between tumour types.

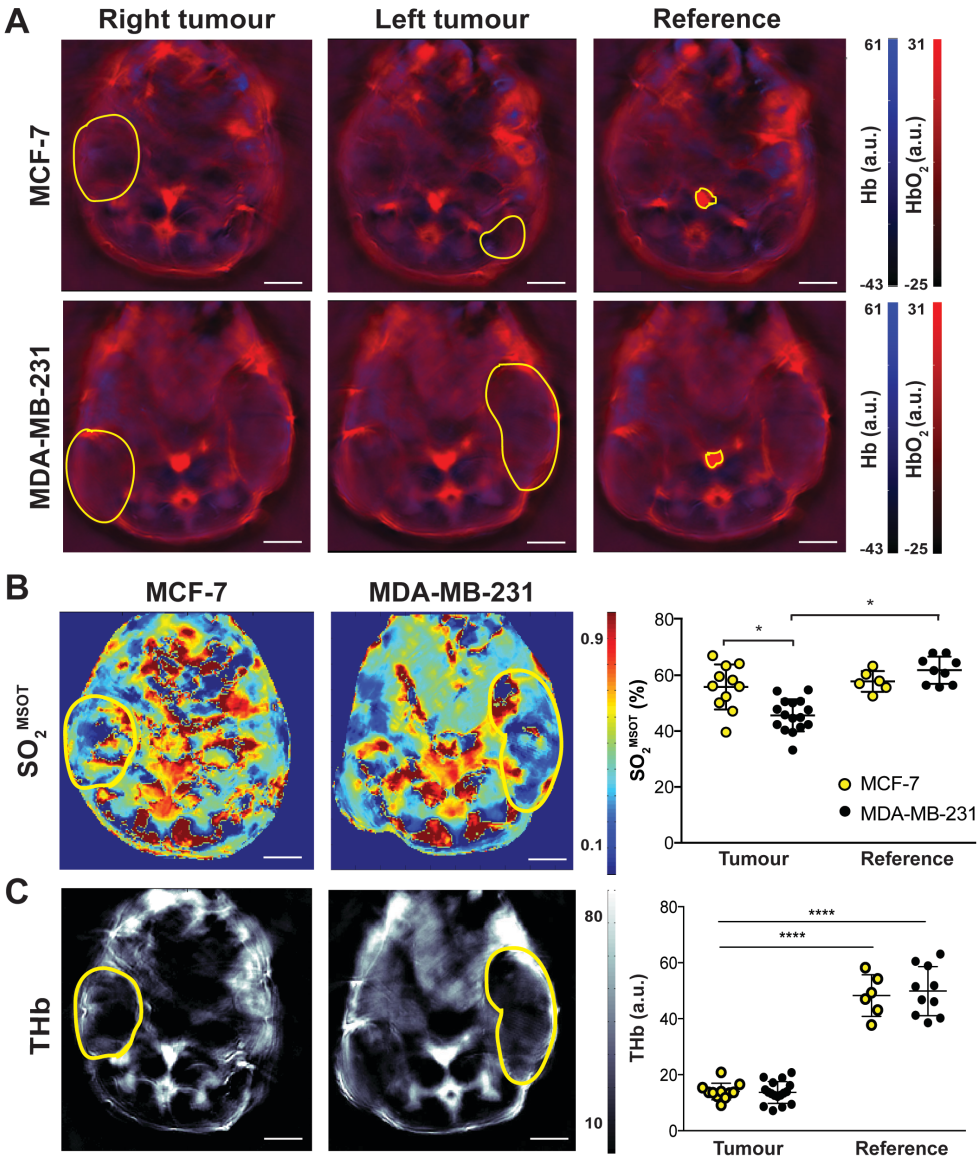
A
Right tumour
Left tumour
Reference
MCF-7
MDA-MB-231
61
31
-43
-25
Hb (a.u.)
HbO2 (a.u.)
B
MCF-7
MDA-MB-231
SO2 MSOT
0.9
0.1
SO2 MSOT (%)
80
60
40
20
0
*
*
MCF-7
MDA-MB-231
Tumour
Reference
C
THb
80
10
THb (a.u.)
****
****
Tumour
Reference

Figure 2: Optoacoustic tomography provides a non-invasive assessment of the rim-core vascular phenotypes of both breast cancer models. (A) Rim data were taken from a region of interest drawn around the outside of the tumour, then shrunk by a radial distance of 1 mm. Significant differences in THb and SO_2^{MSOT} were seen between the rim and core of MDA-MB-231 tumours, though only THb showed a rim-core variation in MCF-7 tumours (B,C). Extracting "large" (20-30 mm^2 OT area) tumours for a size matched analysis (D) showed similar THb values but different SO_2^{MSOT} between rims and cores (E,F). Statistical significance was assessed by paired 2-tailed t-test within a single tumour type and by unpaired 2-tailed t-test between tumour types. For (B) and (C) $n^{MCF\text{-}7}$ = 11; n^{231} = 15, for (E) and (F) $n^{MCF\text{-}7}$ and n^{231} = 4. All panels data expressed as mean±SEM. * p<0.05, ** p<0.01, *** p<0.001, **** p<0.0001.

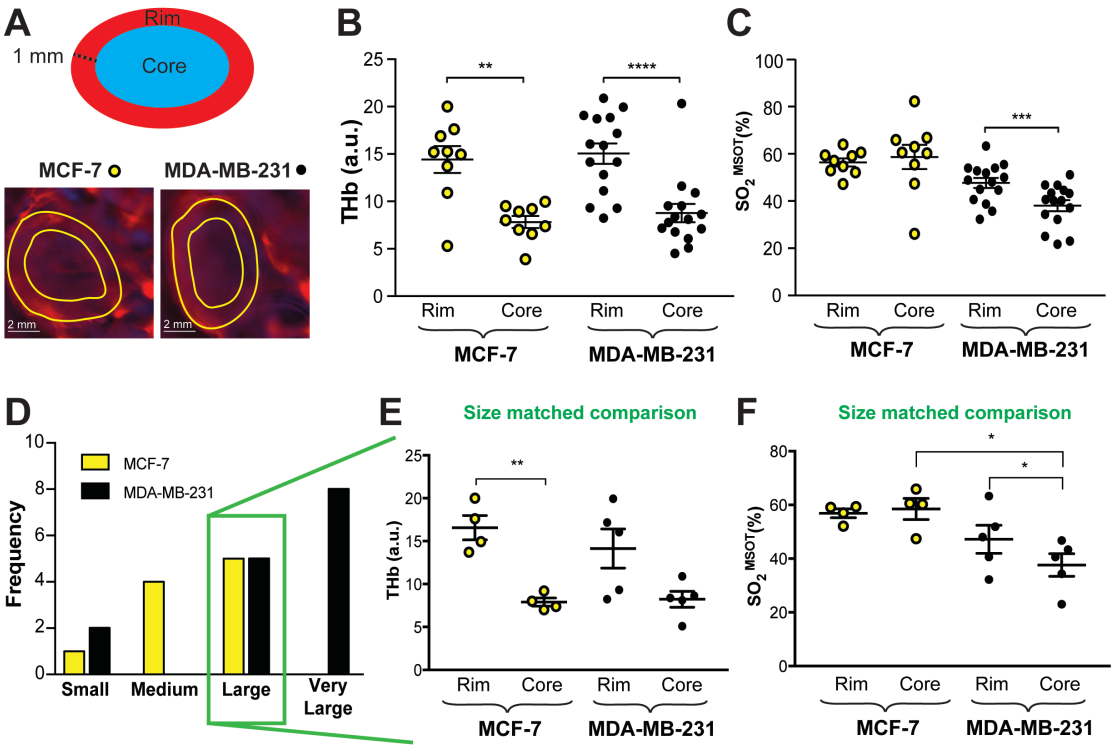

Figure 3: MDA-MB-231 exhibit a high microvessel density but relatively poor maturity compared to MCF-7. (A) IHC representative micrographs for each tumour type stained with CD31 to mark endothelial cells and ASMA to mark the supporting pericyte layer (ASMA+ cells surrounding blood vessels). The lowest panel shows the mask used to count co-localised ASMA and CD31 staining on adjacent sections (orange overlap/ yellow CD31+ only) Arrowheads indicate CD31+ with no ASMA staining in MDA-MB-231. Scale bar = 30 μm. MDA-MB-231 tumours show increased overall CD31 staining (B) and microvessel density (MVD, C), but decreased vessel thickness (D) and ASMA coverage (E) compared to MCF-7. For B, C and D, $n^{MCF\text{-}7}$=12 and n^{231}=16. For E, $n^{MCF\text{-}7}$=7 and n^{231}=4. All panels, data expressed as mean±SEM. *** p<0.001, **** p<0.0001 by unpaired 2-tailed t-test.

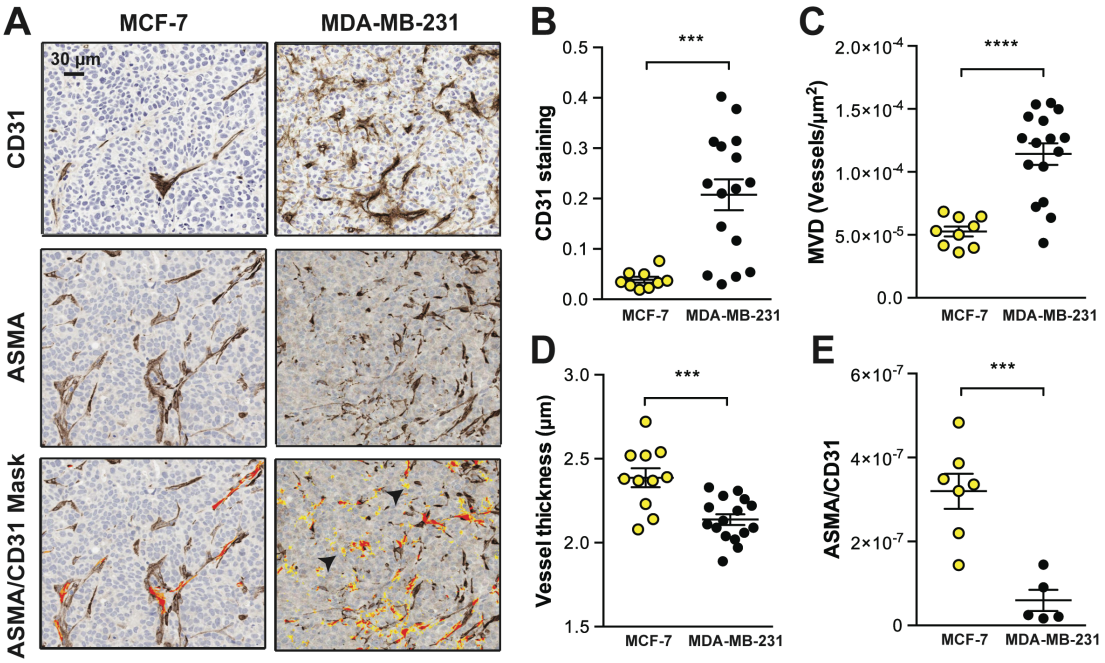

Figure 4: The hypoxic and inflammatory phenotype differs between the two breast tumour models. MDA-MB-231 cells have a lower oxygen consumption rate (A) yet show higher hypoxia in tumours (B). VEGF staining is lower in MDA-MB-231 tumours (C). Serum mouse VEGF (mVEGF, D) and nitric oxide (NO, E) are also lower in MDA-MB-231 tumours. (F) MCF-7 show an inflammatory phenotype, with higher staining for iNOS and Arginase indicating the presence of type 1 and 2 macrophages respectively. Scale bars in (B) and (C) = 50 μm; (F) = 20 μm. For B) and C) $n^{MCF\text{-}7}$=12 and n^{231}=16. For D) and E) $n^{MCF\text{-}7}$=6 and n^{231}=9. All panels, data expressed as mean±SEM, *p<0.05, ** p<0.01, *** p<0.001, **** p<0.0001 by unpaired 2-tailed t-test.

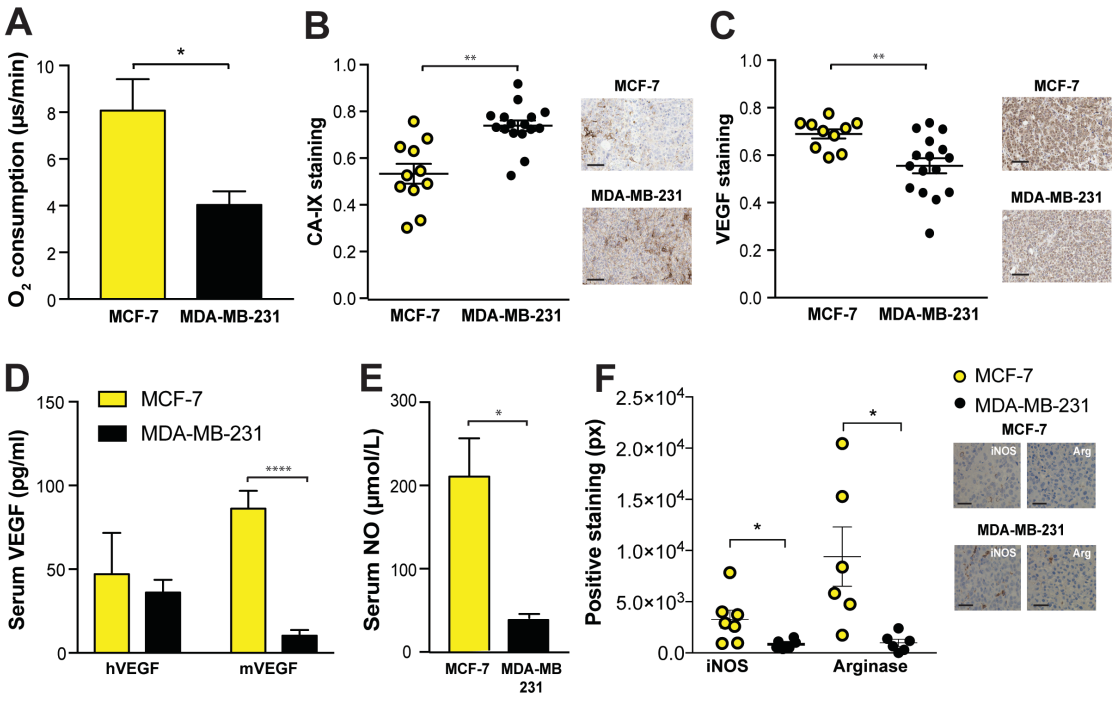

Figure 5: Assessment of vascular mimicry. (A) Representative micrographs (magnification 20x) of tubular-like structures generated in matrigel 3D *in vitro* culture for MDA-MB-231 cells; no such structures are observed in MCF-7 cells. This phenotype is associated with vascular mimicry. (B) Representative micrographs (magnification 40x) of tumour sections stained with PAS and CD31. (C) All PAS-positive blood vessels were identified and the CD31 positivity of these blood vessels was then evaluated. The number of CD31+/PAS+ blood vessels was significantly lower in MDA-MB-231 compared to MCF-7 tumours. (D) Western-blot for protein levels of VE-Cadherin in MCF-7 and MDA-MB-231 xenograft tumours *ex vivo* provided confirmation of these *in vitro* findings. GAPDH is shown as a house-keeping protein. (B) and (C) $n^{MCF\text{-}7}=6$ and $n^{231}=6$ data expressed as mean±SEM, *$p<0.05$ by unpaired 2-tailed t-test. (D) $n^{MCF\text{-}7}=8$ and $n^{231}=15$.

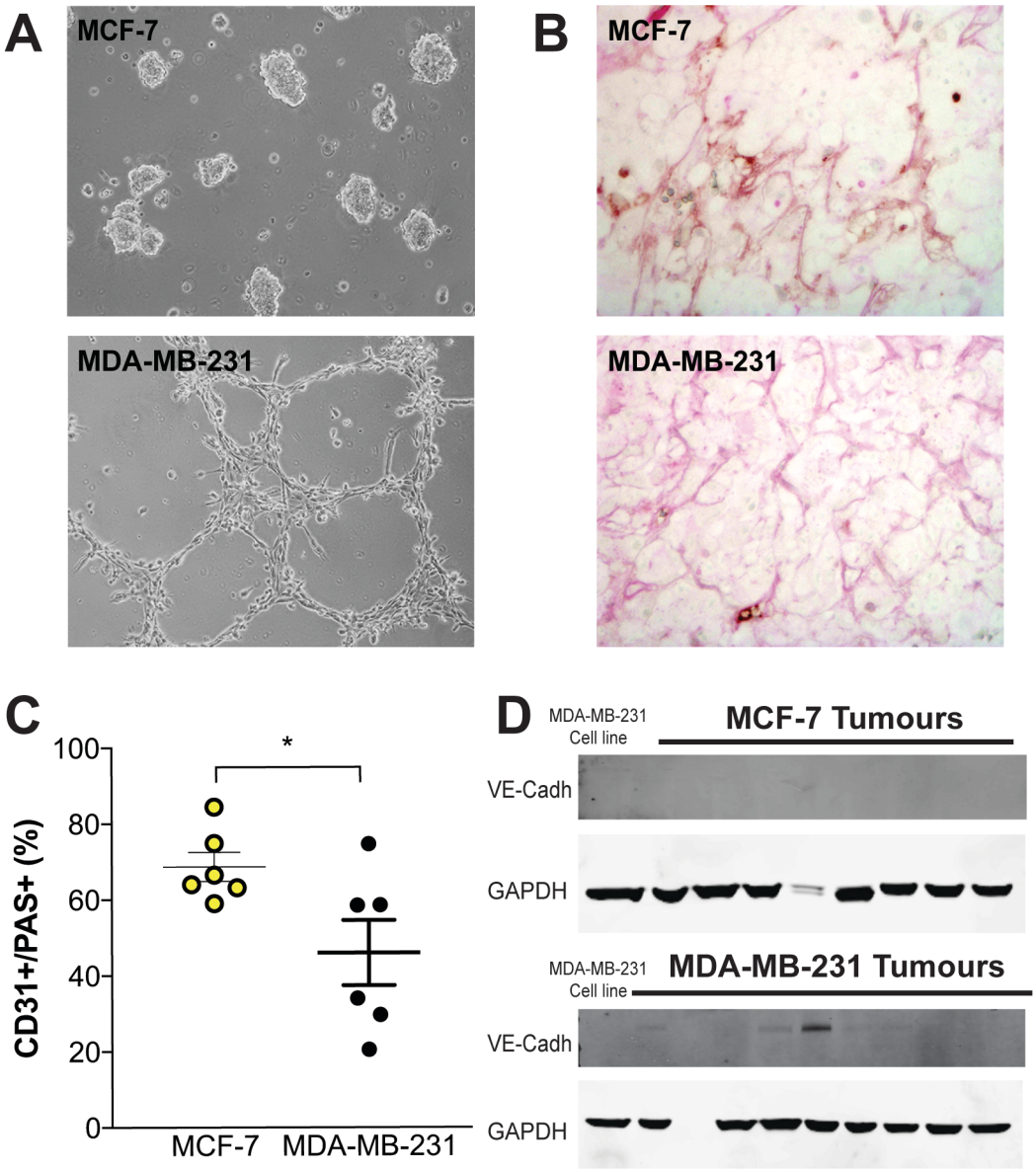
A
MCF-7
MDA-MB-231
B
MCF-7
MDA-MB-231
C
CD31+/PAS+ (%)
100
80
60
40
20
0
*
MCF-7
MDA-MB-231
D
MDA-MB-231
Cell line
MCF-7 Tumours
VE-Cadh
GAPDH
MDA-MB-231
Cell line
MDA-MB-231 Tumours
VE-Cadh
GAPDH

730

Supplementary Information for:

Optoacoustics delineates murine breast cancer models displaying angiogenesis and vascular mimicry

Isabel Quiros-Gonzalez, Michal R Tomaszewski, Sarah Aitken, Laura Ansel-Bollepalli, Leigh-Ann McDuffus, Michael Gill, Lina Hacker, Joanna Brunker and Sarah E. Bohndiek.

Contents

Supplementary Methods

Cell lines

In vitro experiments were performed when cells were between passage 20-25 for both MCF-7 and MDA-MB-231. Authentication using Genemapper ID v3.2.1 (Genetica) by STR Genotyping (1/2015) showed 100% match with the reference sequence in both cases. Cells were maintained in DMEM supplemented by 10% of FBS at 37ºC in 5% CO_2. Oxygen consumption was measured using the MitoXpress Xtra Oxygen Consumption assay.

MitoXpress Xtra Oxygen Consumption assay

Oxygen consumption of the MCF-7 and MDA-MB-231 cells was assessed by the *MitoXpress Xtra Oxygen Consumption (HS Method)* assay (LuxCel Bioscience). Cells were seeded into a 96-well plate in 2 concentrations (50,000 and 100,000 cells/well, n=15) in 150 µL of complete media. The next day MitoXpress Xtra was added to each well in fresh media following manufacturer instructions. Two drops of HS mineral oil were added to each well to prevent oxygen exchange. Positive and negative controls included 1 mg/mL of Glucose Oxidase, 1 µL of 150 µM Carbonyl cyanide-4-(trifluoromethoxy)phenylhydrazone (FCCP) (Sigma Aldrich) solution and 1 µL of 150 µM Antimycin A respectively. Measures were taken at 37°C for 2.5 h in a plate reader (CLARIOstar, BMG Labtech) according to a protocol described elsewhere (Hynes *et al*, 2013). The slopes of fluorescent lifetime changes were extracted for each cell line and cell density were extracted as a quantification of the oxygen consumption in the well.

A duplicate plate was used to quantify the relative cell densities in the wells. The plate without media was frozen at -80°C. After thawing 50 µL of TNE buffer (Tris 50 mM, NaCl 100mM and EDTA 0.1 mM) buffer with 20 µg/mL Hoechst 33342 was added to each well and incubated for 15 minutes at room temperature. The plate was scanned at 361 nm excitation and 497 nm emission (CLARIOstar, BMG Labtech) and the fluorescence signal intensity was used as a measure of the cell density.

Measurements of oxidative modification

For blood nitration content, terminal blood collection was performed in heparinised tubes. Samples were centrifuged and diluted for quantification with Parameter™ Total Nitric Oxide (NO) and Nitrate/Nitrite Assay (R&D) following manufacturer's instructions. The detection is based on the colorimetric detection of nitrite by the Griess Reaction. Optical densities at 540 nm (signal) and 690 nm (correction) were detected and the relative concentration of NO was extrapolated from a standard curve.

For detection of the redox modified nucleotide 8-hydroxy-2'deoxyguanosine, we purified the DNA from paraffin embedded tumour tissue and detected the modification by ELISA. Briefly, DNA from 3-5 sections (5µm thickness) were extracted by using the PaxGene DNA kit (Qiagen) following the manufacturer's instructions. For all the tumours 2 µg of DNA were loaded into each well for the immunodetection using HT 8-oxo-dG ELISA kit II (Trevigen) following manufacturer's instructions.

Western-blot for nitrotyrosine and VE-cadherin

Tissue was homogenised and lysed with Pierce® RIPA buffer (Thermo Scientific) plus Halt protease and phosphatase inhibitors cocktail (Thermo Scientific). Protein concentration was determined by using the Direct Detect system (Millipore) and 45 µg of protein was loaded for electrophoresis. Proteins were dry-transferred to a PDVF membrane using iBLOT2.0 system. For nitrotyrosine, all tumour samples were compared with an extract from MDA-MB-231 cells treated with peroxynitrite 10 µM ($ONOO^-$) taken as a reference. Quantification was performed for the whole lane. For VE-Cadherin only presence- absence was assessed. GAPDH was used as house-keeping protein. Antibodies and conditions: Anti-Nitrotyrosine (Cayman Chemical) (1:300), anti-VE-Cadherin (1:1000) and anti-GAPDH (1:5000) (both Cell Signalling Technologies) were incubated overnight at 4 °C. Secondary antibodies were anti-Rabbit IRDye® 680LT (LI-COR) and anti-Mouse IRDye® 680LT (both 1:15000). Band intensity quantification was performed using Image J. For nitrotyrosine, all bands detectable from ~35 KDa to 100 KDa were measured and normalised against GAPDH. For VE-Cadherin, only the presence or absence of signal was counted.

Immunohistochemistry and special staining

Tissues were collected and fixed in 4% PFA for 24h. Samples were processed by the Cancer Research UK Cambridge Institute Histopathology Core. Tumour tissues were embedded in paraffin, sectioned and rehydrated. Immunohistohemistry for CD31, alpha Smooth Muscle Actin (aSMA), oestrogen receptor (OR), Vascular Endothelial Growth Factor (VEGF) and Carbonic Anhydrase IX (CA-IX) was performed in a BOND automated stainer (Leica Biosystems) at the following concentrations 1:50, 1:500, 1:200, 1:250 and 1:1000. All the antibodies needed from antigen retrieval. Antigen retrieval was performed previous to primary antibody incubation as follows: Proteinase K 10' at 37ºC for CD31, Tris-EDTA Heat shock for aSMA and Sodium Citrate heat shock for OE, VEGF and CA-IX. Toluidine blue for mast cells staining was performed following standard protocols.

Immunohistochemistry for Arginase and inducible Nitric Oxide Synthase (iNOS both Abcam) was performed manually. Briefly, after deparaffination and rehydration slides underwent antigen retrieval (10 mM Citrate buffer, 20 min, 95 °C), samples were blocked for 30 min using the Endogenous Blocking reagent (Dako). Primary antibodies anti-Arginase (1:200) and anti-iNOS (1:400) were diluted in 1% Cold Water Fish Skin gelatine in PBS and incubated for 40 minutes at room temperature. After serial washes (2x 5 min, PBS) the slides were incubated with the secondary anti-Rabbit+anti-Mouse HRP-conjugated solution (Dako) for 30 min. Di-amino-benzidine (DAB) was used as a substrate.

For Periodic Acid Schiff (PAS) staining alone, slides rehydrated were incubated in α-amilase for 30 min. After washing, slides were incubated in Acid Schiff for 5 min and subsequently in Schiff Reagent for another 15 min. Light Haematoxylin (40 s) was used as counterstain. Results are shown in Supplementary Figure 5. For Periodic Acid Schiff (PAS) staining with CD31, slides rehydrated were incubated in were incubated in Acid Schiff for 5 min and subsequently in Schiff Reagent for another 15 min. Light Haematoxylin (40 s) was used as counterstain. When indicated, after PAS staining slides were treated with Proteinase K at 37 °C for 10 minutes and blocked with the endogenous blocking solution

(Dako) and incubated with CD31 (1:100). The secondary anti-Rabbit+anti-Mouse HRP-conjugated solution (Dako) was incubated for 30 min. Di-amino-benzidine (DAB) was used as a substrate.

Mouse and human VEGF inmunodetection in serum

For mouse and human VEGF immunodetection (mVEGF and hVEGF respectively) Quantikine® ELISA kits (R&D) were used. Plasma samples were diluted 1:10 and 50 µl were used to quantify the concentration added per well. The procedure was carried out following manufacturers instructions. The colorimetric reaction was quantified at 450 nm. The final concentrations were extrapolated by correlation of the log of the O.D. with the log of the values in the standard curve.

Supplementary Figures

Figure S1: Proliferation characteristics of MCF-7 and MDA-MB-231. (A) MCF-7 tumours were studied up to 7 weeks post inoculation, after which mice had to be sacrificed due to side effects from the implanted oestrogen pellet. (B) MDA-MB-231 tumours were studied up to 12 weeks post inoculation, after which mice were sacrificed due to ethical animal welfare limits. (C, D) Individual growth curves for both MCF-7 and MDA-MB-231 tumours. (E) H&E sections were used to identify the necrotic areas; a magnification of a field showing representative necrotic areas is shown (left) together with a quantification of the necrotic area (right). (F) Oestrogen receptor (OR) status was confirmed in MCF-7 tumours, with negligible oestrogen positive nuclei observed in MDA-MB-231 assessed by unpaired t-test. Assessment of tumour volume by calipers (as shown in A-D) was compared to assessment using the largest observable tumour area within a single optoacoustic tomography (OT) slice and showed a significant positive Pearson correlation for MCF-7 (G) and MDA-MB-231 (H). For (A-D) n^{MCF-7} =11, for (E,F) n^{MCF-7}=12. All panels n^{231}=16, data expressed as mean±SEM. ** p<0.01, *** p<0.001, **** p<0.0001.

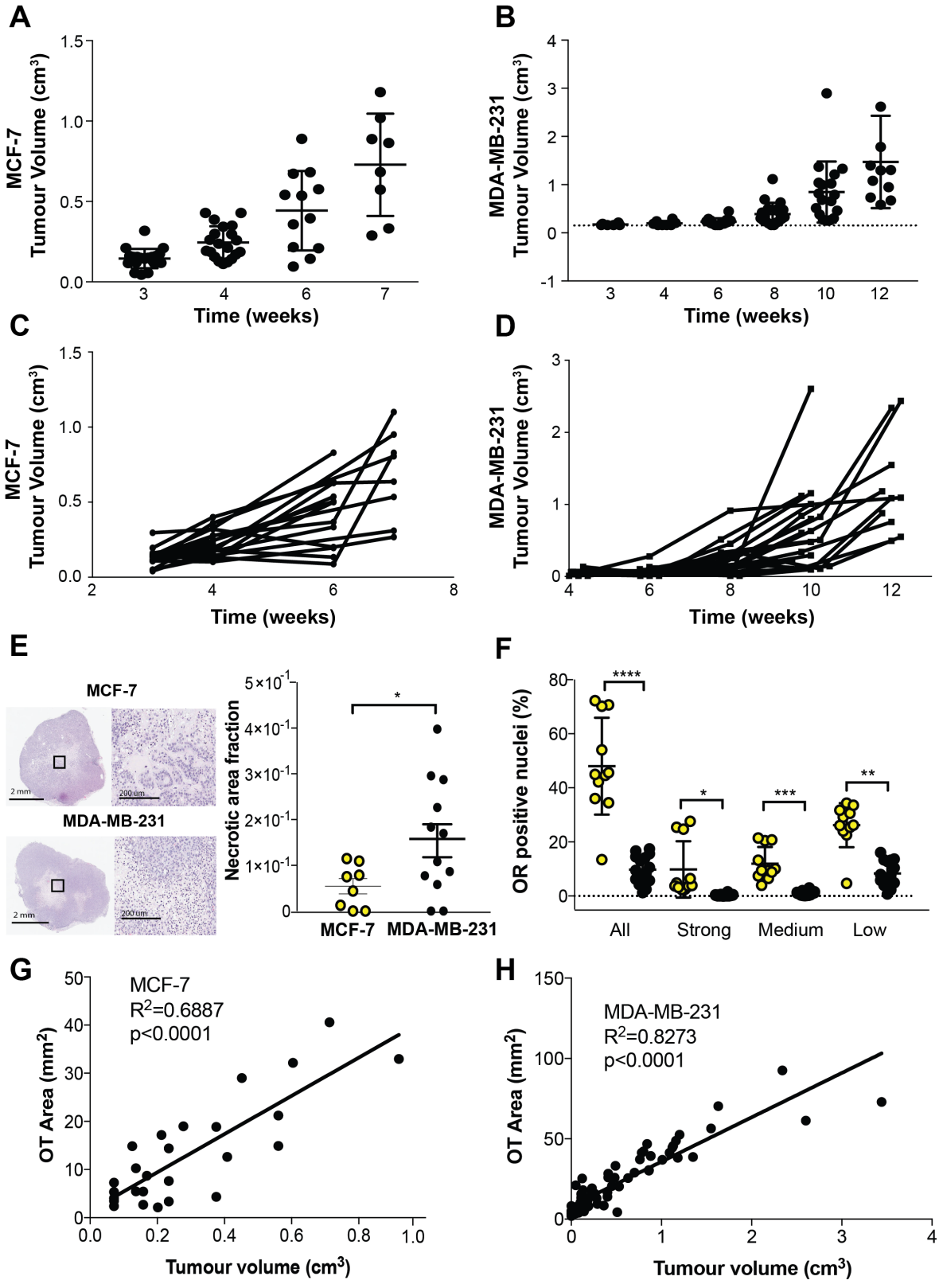
A
MCF-7
Tumour Volume (cm³)
Time (weeks)
B
MDA-MB-231
Tumour Volume (cm³)
Time (weeks)
C
MCF-7
Tumour Volume (cm³)
Time (weeks)
D
MDA-MB-231
Tumour Volume (cm³)
Time (weeks)
E
MCF-7
MDA-MB-231
2 mm
200 um
Necrotic area fraction
MCF-7
MDA-MB-231
F
OR positive nuclei (%)
All
Strong
Medium
Low
G
MCF-7
R²=0.6887
p<0.0001
OT Area (mm²)
Tumour volume (cm³)
H
MDA-MB-231
R²=0.8273
p<0.0001
OT Area (mm²)
Tumour volume (cm³)

Figure S2: Optoacoustic tomography allows longitudinal monitoring of oxygenation and total haemoglobin. (A) The coefficient of variation (COV) was assessed for measurements of oxygen saturation (SO_2^{MSOT}), total haemoglobin (THb), deoxyhaemoglobin (Hb) and oxyhaemoglobn (HbO_2). Data were extracted from regions of interest placed over MCF-7 and MDA-MB-231 tumours, as well as from the reference area (Ref), in mice imaged repeatedly at 3 time points (0h, 24h, and 48h). COV values for MDA-MB-231 tumours are: 6.5±2.8% (SO_2^{MSOT}), 28.3±25.2% (THb), 51.7±22.6% (Hb) and 39.5±23.1% (HbO_2). COV values for MCF-7 tumours are: 5.0±1.6% (SO_2^{MSOT}), 11.4±0.9% (THb), 17.8±4.5% (Hb) and 15.5±3.5% (HbO_2). COV values for the reference are: 3.1±1.8% (SO_2^{MSOT}), 10.1±3.4% (THb), 21.6±13.6% (Hb) and 8.8±3.9% (HbO_2). (B) SO_2^{MSOT} shown over the time course of the experiment. SO_2^{MSOT} remains approximately constant in the MDA-MB-231 tumour region over time from study initiation, whereas a trend towards decreasing oxygenation is observed in MCF-7. (C) These trends remain when the oxygenation signal from the tumour (tum) is normalised to that extracted from the reference region around the aorta and inferior vena cava (ref). Normalisation was performed to ensure that any changes in systemic blood oxygenation were not affecting our results. (D) No significant change THb was observed across the time course. All panels data expressed as mean±SEM. * $p<0.05$, ** $p<0.01$, *** $p<0.001$, **** $p<0.0001$. (A) $n^{MCF-7}= 3$, $n^{231} = 4$ and $n^{reference} = 3$. (B) (C) and (D) $n^{MCF-7} = 11$ and $n^{231} = 16$.

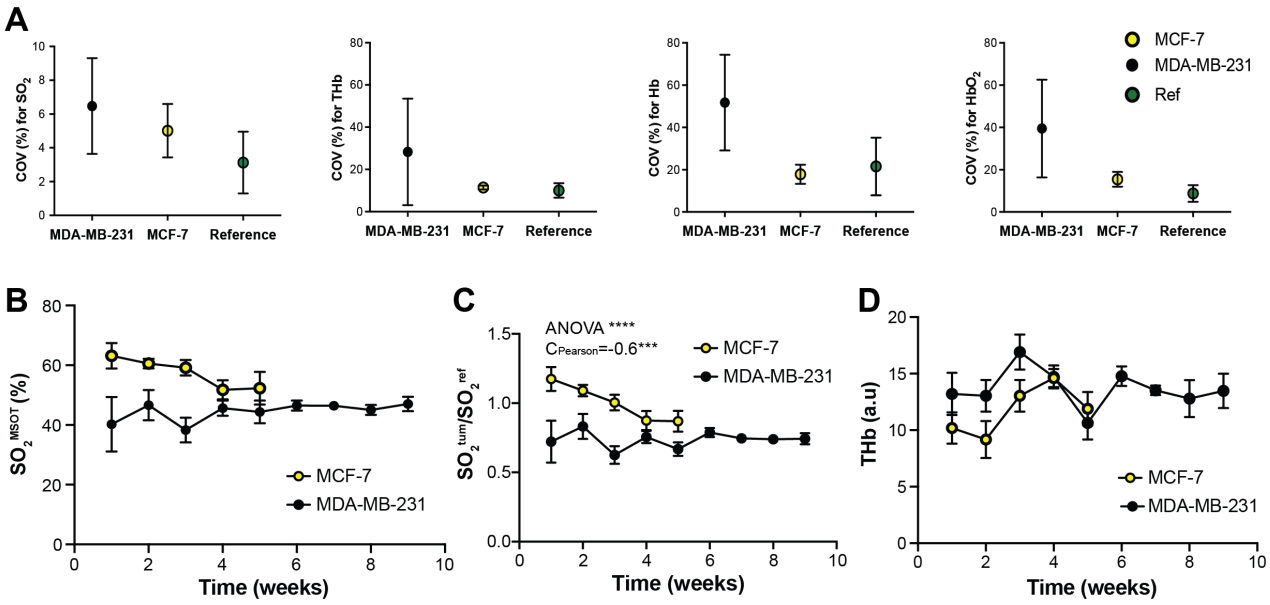
A
COV (%) for SO2
COV (%) for THb
COV (%) for Hb
COV (%) for HbO2
MDA-MB-231
MCF-7
Reference
MCF-7
MDA-MB-231
Ref
B
SO2 MSOT (%)
Time (weeks)
C
ANOVA ****
CPearson=-0.6***
SO2 tum/SO2 ref
D
THb (a.u)

Figure S3: Deoxyhaemoglobin (Hb) and oxyhaemoglobin (HbO_2) signals used to compute total haemoglobin and oxygen saturation in the tumour rim and core. (A, B) Data pooled for all tumours that underwent OT. (C, D) Data from size matched comparison. (E) Rim and core analysis for SO_2^{MSOT} during time, tumours were analysed after they were sufficiently large to enable a 1 mm radius region of interest to be drawn to denote the rim. Statistical significance was assessed by paired t-test within a single tumour type and by unpaired t-test between tumour types. For (A) and (B) and (E) $n^{MCF\text{-}7} = 11$; $n^{231} = 15$, for (C) and (D) $n^{MCF\text{-}7}$ and $n^{231} = 4$. All panels data expressed as mean±SEM. * $p<0.05$, ** $p<0.01$, *** $p<0.001$, **** $p<0.0001$.

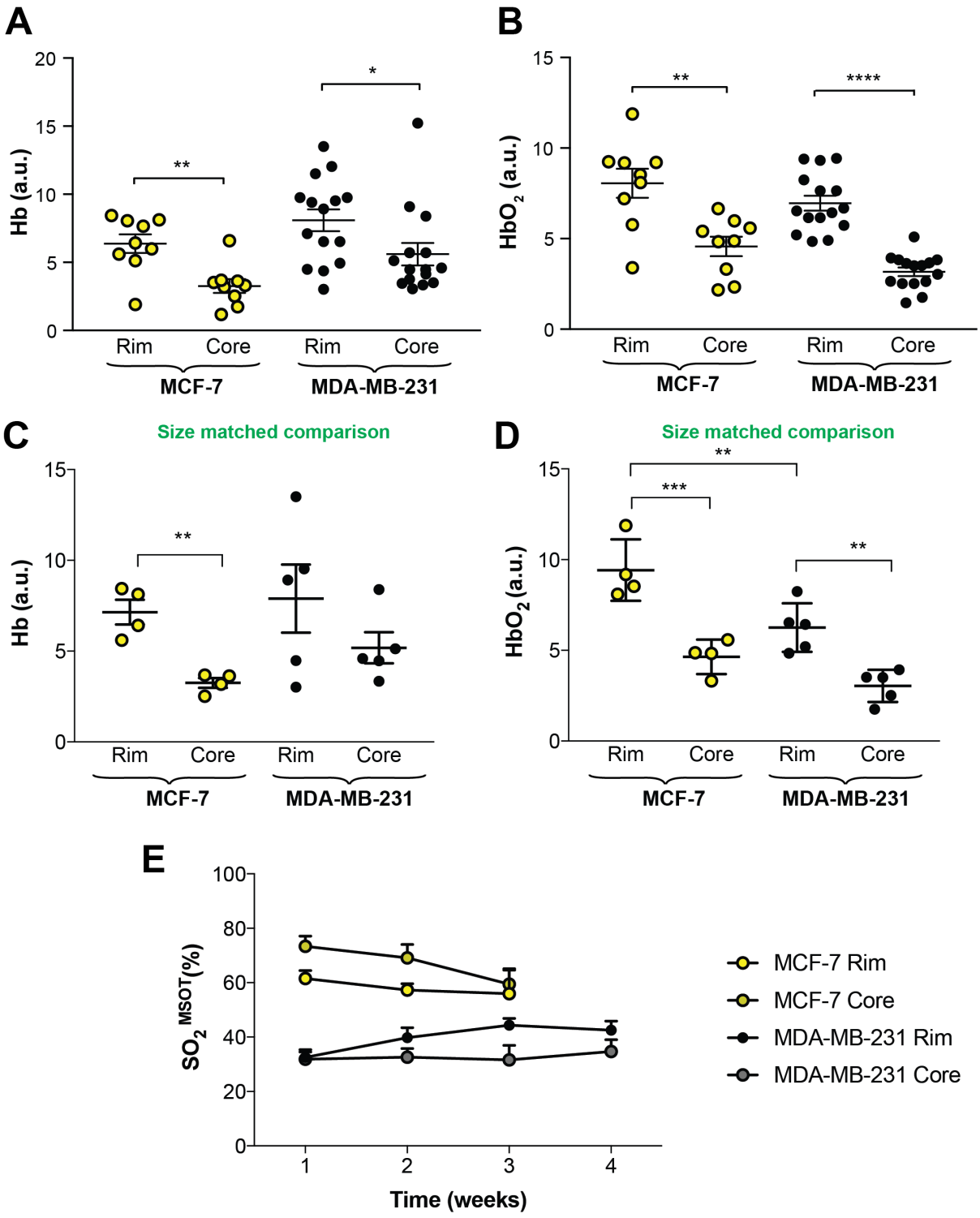
A
Hb (a.u.)
20
15
10
5
0
**
*
Rim
Core
Rim
Core
MCF-7
MDA-MB-231
B
HbO2 (a.u.)
15
10
5
0
**
****
Rim
Core
Rim
Core
MCF-7
MDA-MB-231
C
Size matched comparison
Hb (a.u.)
15
10
5
0
**
Rim
Core
Rim
Core
MCF-7
MDA-MB-231
D
Size matched comparison
HbO2 (a.u.)
15
10
5
0
**
***
**
Rim
Core
Rim
Core
MCF-7
MDA-MB-231
E
SO2 MSOT(%)
100
80
60
40
20
0
1
2
3
4
Time (weeks)
MCF-7 Rim
MCF-7 Core
MDA-MB-231 Rim
MDA-MB-231 Core

Figure S4: Inflammatory and oxidative stress markers. (A) Representative image of nitrotyrosilation detection in tumour proteins by western-blot. GADPH was used as a housekeeping protein. (B) Relative quantification normalized against a protein extract of MDA-MB-231 cells treated with $ONOO^-$ at 10 µM. No significant difference was observed between the two models. (C) ELISA quantification of oxidative modification of DNA 8-oxo-dG in tumour tissue. (A) and (B) $n^{MCF-7} = 8$; $n^{231} = 15$. $n^{MCF-7} = 10$; $n^{231} = 15$).

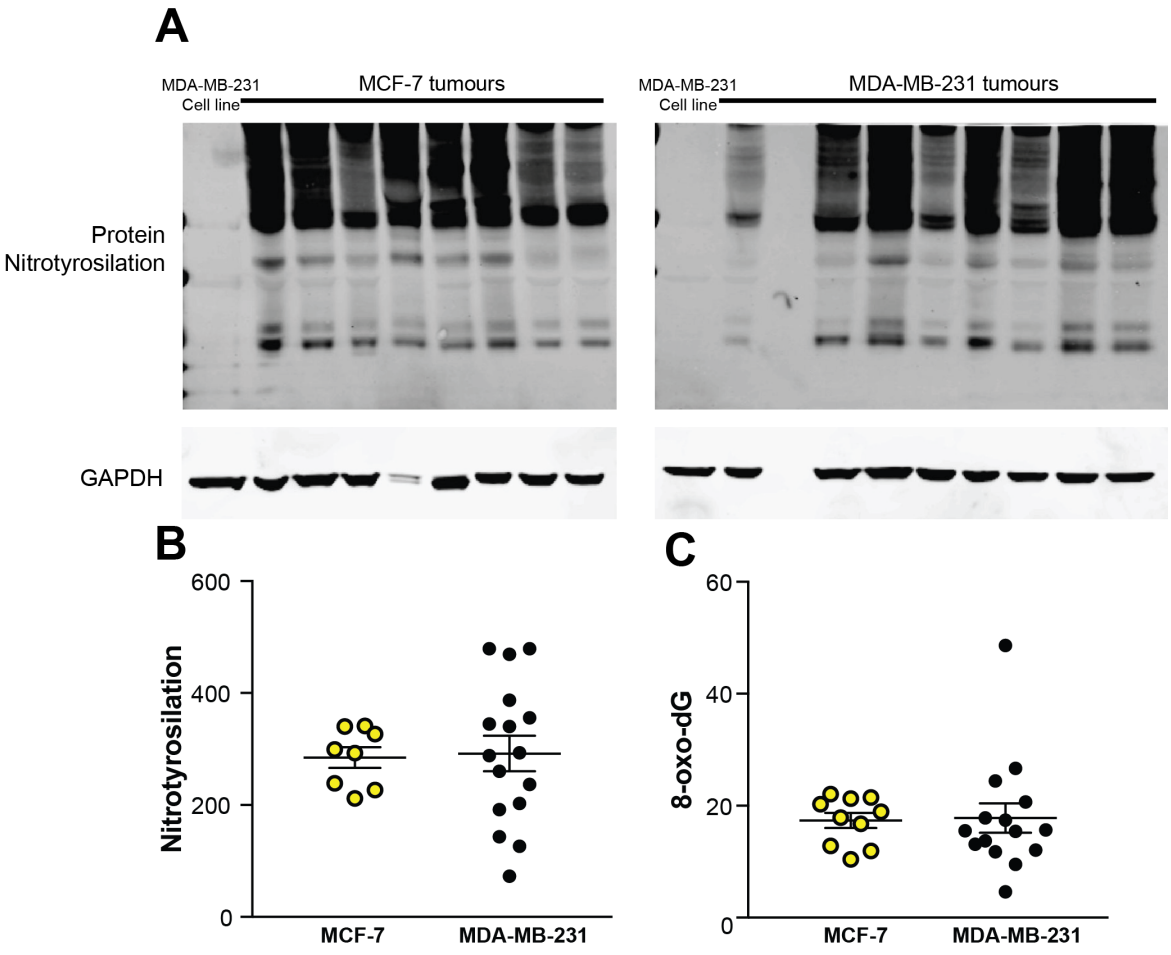

Figure S5: Quantification of PAS and CD31 staining in adjacent sections. (A) Representative micrographs of MCF-7 and MDA-MB-231 tumours (magnification 20x) stained with PAS and immunostained for CD31 in serial sections. Blood vessels were identified in PAS staining (yellow marks) and the corresponding region was located in the CD31 immunostaining. Blood vessels with positive (green) and negative (arrowhead) CD31 staining are marked. (B) Quantification of the CD31+ staining in blood vessels. $n^{MCF\text{-}7}$=6 and n^{231}=6 data expressed as mean±SEM, *p<0.05 by unpaired 2-tailed t-test.